Combined Scanning Probe Nanotomography and Optical Microspectroscopy: A Correlative Technique for 3D Characterization of Nanomaterials

Konstantin E. Mochalov,[†,‡] Anton E. Efimov,[§,⊥] Alexey Bobrovsky,[∥] Igor I. Agapov,[§] Anton A. Chistyakov,[†] Vladimir Oleinikov,[†,‡] Alyona Sukhanova,[†,#] and Igor Nabiev[†,#,*]

[†]Laboratory of Nano-bioengineering, National Research Nuclear University "Moscow Engineering Physics Institute", 115409 Moscow, Russian Federation, [‡]Laboratory of Biophysics, Shemyakin–Ovchinnikov Institute of Bioorganic Chemistry, Russian Academy of Sciences, 117997 Moscow, Russian Federation, [§]Laboratory of Bionanotechnology, Shumakov Federal Research Center of Transplantology and Artificial Organs, 123182, Moscow, Russian Federation, [⊥]SNOTRA, LLC., 105318 Moscow, Russian Federation, [∥]Faculty of Chemistry, Moscow State University, 119991 Moscow, Russian Federation, and [#]Laboratory of Research in Nanosciences - EA4682, Université de Reims Champagne-Ardenne, 51100 Reims, Champagne-Ardenne, France. All the authors contributed to the writing of the manuscript. All authors have given approval to the final version of the manuscript.

ABSTRACT Combination of 3D structural analysis with optical characterization of the same sample area on the nanoscale is a highly demanded approach in nanophotonics, materials science, and quality control of nanomaterial. We have developed a correlative microscopy technique where the 3D structure of the sample is reconstructed on the nanoscale by means of a "slice-and-view" combination of ultramicrotomy and scanning probe microscopy (scanning probe nanotomography, SPNT), and its optical characteristics are analyzed using microspectroscopy. This approach has been used to determine the direct quantitative relationship of the 3D structural characteristics of nanovolumes of materials with their microscopic optical properties. This technique has been applied to 3D structural and optical characterization of a hybrid material consisting of cholesteric liquid crystals doped with fluorescent quantum dots (QDs) that can be used for photochemical patterning and image recording through the changes in the dissymmetry factor of the circular polarization of QD emission. The differences in the polarization images and fluorescent spectra of this hybrid material have proved to be correlated with the arrangement of the areas of homogeneous distribution and heterogeneous clustering of QDs. The reconstruction of the 3D nanostructure of the liquid crystal matrix in the areas of homogeneous QDs distribution has shown that QDs do not perturb the periodic planar texture of the cholesteric liquid crystal matrix, whereas QD clusters do perturb it. The combined microspectroscopy–nanotomography technique will be important for evaluating the effects of nanoparticles on the structural organization of organic and liquid crystal matrices and biomedical materials, as well as quality control of nanotechnology fabrication processes and products.

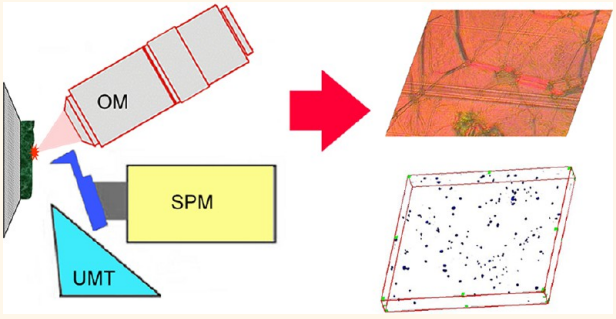

KEYWORDS: scanning probe microscopy · nanotomography · 3D structural analysis · optical microspectroscopy · liquid crystals matrix · fluorescent quantum dots

Simultaneous study of the nanoscale structural properties of materials and quantitative assessment of their relationship with the micro- or macroscopic functional properties of the materials are crucial prerequisites for further development of modern nanotechnological products and processes of nanofabrication.[1−3] One of the most rapidly growing areas of nanotechnological applications is related to the exploration of unique optical properties of some nanomaterials that can be used in nano-optoelectronics,[4] nanophotonics,[5] diagnostics,[6] and drug delivery.[7] Engineering of nanomaterials with controlled optical properties requires the evaluation of the relationship between the nanoscale 3D morphology of the sample and its microscopic optical properties,[3] whereas the biomedical applications and nanotoxicity studies require

* Address correspondence to igor.nabiev@gmail.com.

Received for review July 7, 2013 and accepted August 30, 2013.

Published online August 30, 2013
10.1021/nn403448p

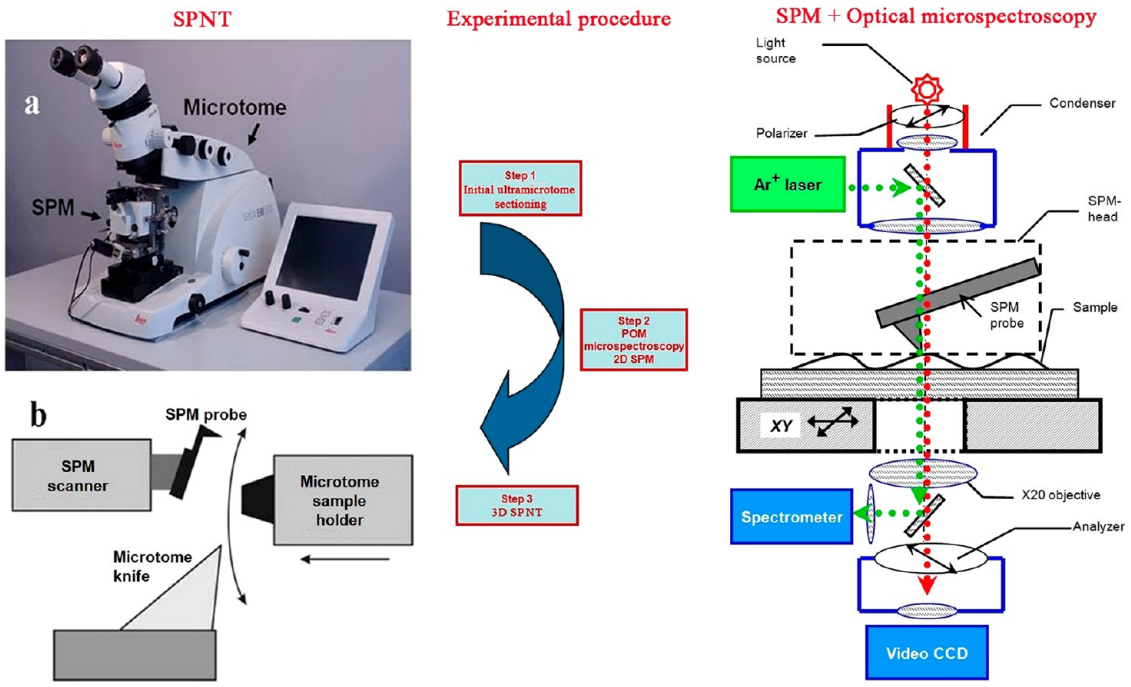

Figure 1. Experimental apparatus and procedure of the SPNT−OM technique allowing for surface probe microscopy (SPM), transmitting optical microscopy (OM), and fluorescence microspectroscopy measurements, as well as the 3D reconstruction of the sample structure by means of SPNT for the same region of the sample. Left: (a) The overview of the SPNT setup. (b) The schematic diagram of the SPNT system operation. Right: The layout of the combined apparatus for complementary SPM, OM, and confocal microscopy measurements.

the nanoscale 3D morphological analysis of tissues and cells in parallel with the fluorescent analysis of the spatial distribution of diagnostic or therapeutic nanoprobes in them.[8] Although a variety of advanced optical,[9] electron,[10] and scanning probe[11] microscopic techniques have been developed during the past decades, it is clear that no single microscopic technique can provide the comprehensive understanding of ultrastructure that is necessary for solving these tasks; hence, complementary multimodal techniques are called for.

In this paper, we report on the development of a correlative technique combining "slice-and-view" scanning probe nanotomography (SPNT) with optical microspectroscopy (OM) that makes it possible to quantitatively correlate the local properties and structural characteristics of a material on the nanoscale with its microscopic optical properties and use this correlation for the analysis of a hybrid nanophotonic material engineered from cholesteric liquid crystals and semiconductor fluorescent quantum dots (QDs). This hybrid material has proved to be promising for photochemical patterning and image recording through the changes in the dissymmetry factor of the circular polarization of QD emission.[12−15] The photo- and electroactive materials with a controlled degree of fluorescence polarization may be used as on-demand single-photon sources in photonics, optoelectronics, and quantum cryptography,[16,17] and as a basis for the development of nanophotonic systems capable of low-threshold lasing.[18] A combined SPNT−OM technique permits the quantitative correlation of the arrangement of the areas of homogeneous distribution and heterogeneous clustering of QDs with the differences in the polarization images and fluorescent spectra of materials. This makes it possible to perform quality control of the materials on the nanoscale and optimize the procedure of their nanoengineering.

The strategic nanoscience and nanotechnology trends call for an impetus in the form of a new correlative technique combining 3D high-resolution structural analysis with optical characterization of the same sample areas, which would permit direct quantitative correlation of the nanoscale material structure with its microscopic optical characteristics. Developed here, the correlative SPNT−OM technique is expected to provide important data on the effects of nanoparticles on the structural organization of organic and liquid-crystal matrices and biomedical materials.

RESULTS AND DISCUSSION

We have developed a new analytical SPNT−OM technique that allows correlative SPM, optical microscopy, and fluorescent spectroscopy data to be obtained from the same area of the sample and the 3D nanostructure of the sample to be reconstructed by means of scanning probe nanotomography. The first step (Figure 1) consists of initial ultramicrotome sectioning of the sample placed on a glass substrate in order to obtain a flat block face surface for SPM−OM

correlative microscopy. Then, the sample is transferred to a combined SPM−OM device for atomic force microscopy (AFM) and polarized optical microscopy (POM) imaging and spectroscopic (fluorescent) measurement of the sample. After that, the sample is transferred back to the SPNT system, where we locate the same surface areas on the block face by means of AFM and optical microscopy and then proceed with ultramicrotoming with a controlled uniform thickness of sections followed by AFM measurements to obtain a nanotomographic 3D reconstruction.

We used SPNT−OM correlative microscopy to examine a sample of the nanohybrid material consisting of cholesteric liquid crystal (CLC) matrices doped with fluorescent quantum dots (QDs).[12,13] Glass-forming cyclosiloxane was used as a CLC matrix; it was characterized by a selective light reflection peak for left-handed circularly polarized light at λ = 450 nm, a clearing temperature of 180−182 °C, and a glass transition temperature of approximately 50 °C. Sorb, a derivative of isosorbide and cinnamic acid, was used as a chiral photochromic dopant responsible for helix phototuning properties. This dopant is characterized by a high helical twisting power and capability for inducing the formation of a right-handed supramolecular helical structure in the cholesteric matrix. UV irradiation induces thermally irreversible E−Z isomerization of Sorb at C═C bonds, which is accompanied by a decrease in the helical twisting power.[19] Therefore, introduction of Sorb as a dopant into a cyclosiloxane CLC matrix leads to partial untwisting of the helix and, hence, a red shift of the selective light reflection peak. Subsequent UV irradiation results in a reverse shift of the selective light reflection peak to shorter wavelengths.[20]

To make the CLC material optically active, we used CdSe/ZnS core/shell semiconductor QDs with emission wavelengths at 530 and 604 nm as fluorescent dopants. Incorporation of a small amount of QDs did not change the glass transition temperature of the material (~50 °C), whereas the clearing temperature was shifted to 170−172 °C (10 °C lower than that for a pure CLC matrix).

Initial analysis of the structure of the material using POM did not show any signs of aggregation or phase separation in most of the area of planar films; hence, the obtained composite material was considered sufficiently homogeneous. However, for manufacturing QD−CLC systems with a high concentration of QDs, which is necessary for lasing and other applications, we have to know the true 3D structure of the produced nanocomposites, the maximal achievable concentration of homogeneously distributed QDs in the CLC matrix, and the influence of QD clusters on the optical properties of the QD−CLC hybrid material.

Figure 2a shows a POM image of the ultramicrotomed area of a QD−CLC sample (steps 1 and 2 in Figure 1). It is worth mentioning that POM is a conventional technique for control of the quality of cholesteric LC structures.[21] Ideal LC structures turn transmitting linearly polarized light into elliptically polarized light and, hence, appear as a bright field in POM images (marked with a green circle in Figure 2a), whereas defect areas do not affect light polarization and appear as dark stains in POM images (marked with a blue circle in Figure 2a). The oily streaks seen in Figure 2 are typical defects for such LC structures (even without any dopants),[21] while the defects similar to that marked with a blue circle are specific for QD aggregation.

Then, we recorded and analyzed the microfluorescent spectra of left- and right-handed circularly polarized components of emission from the planar (green circle) and defect (blue circle) areas of the QD−CLC sample (Figure 2b). One can see that the aggregates of QDs causing defects are characterized by fluorescent spectra that are a superposition of the fluorescence emission spectra of QDs embedded in the LC matrix (530 and 604 nm). In contrast, the left-handed circularly polarized component of the fluorescence emission spectrum of nonaggregated QDs is modified by a peak of selective light reflection at 590 nm, which is typical of the "ideal" structure of CLC materials (see above). This modulation is characterized by the fluorescence dissymmetry factor:

$$g_e = 2(I_L - I_R)/(I_L + I_R) \quad (1)$$

where I_L and I_R are, respectively, the left- and right-handed circularly polarized components of the QD fluorescence spectrum.[22] The considerable negative fluorescence dissymmetry factor that can be seen in Figure 2c clearly indicates a regular planar structure of the CLC matrix in this area.

Although these data permitted a clear differentiation between the planar and defect areas of the CLC material, the following questions remained unanswered: (1) Are the QDs in the planar zones located separately from one another, or are they aggregated into microclusters? (2) What are the proportions of QDs homogeneously distributed in the CLC matrix and aggregated in clusters (in other words, what is the QD solubility in the CLC matrix)?

The answers on these questions could be found using the additional advantage of the SPNT−OM technique shown as step 3 in Figure 1 (3D SPNT).

Figure 3 shows the 2D and 3D structural analyses of distributions of QDs in the planar and defect zones of the same area of the CLC matrix. The 2D AFM image (Figure 3a) corresponds to the area within the black square in Figure 2a. The planar and defect areas are quite well distinguished, and the approximate border between the planar and defect areas corresponds to the correlative POM data. Figure 3a demonstrates that QD aggregates are mostly located in the defect area. Some aggregates observed in planar area are located in oily streaks, which are the natural defects of the planar structure. We used the SPNT technique to make

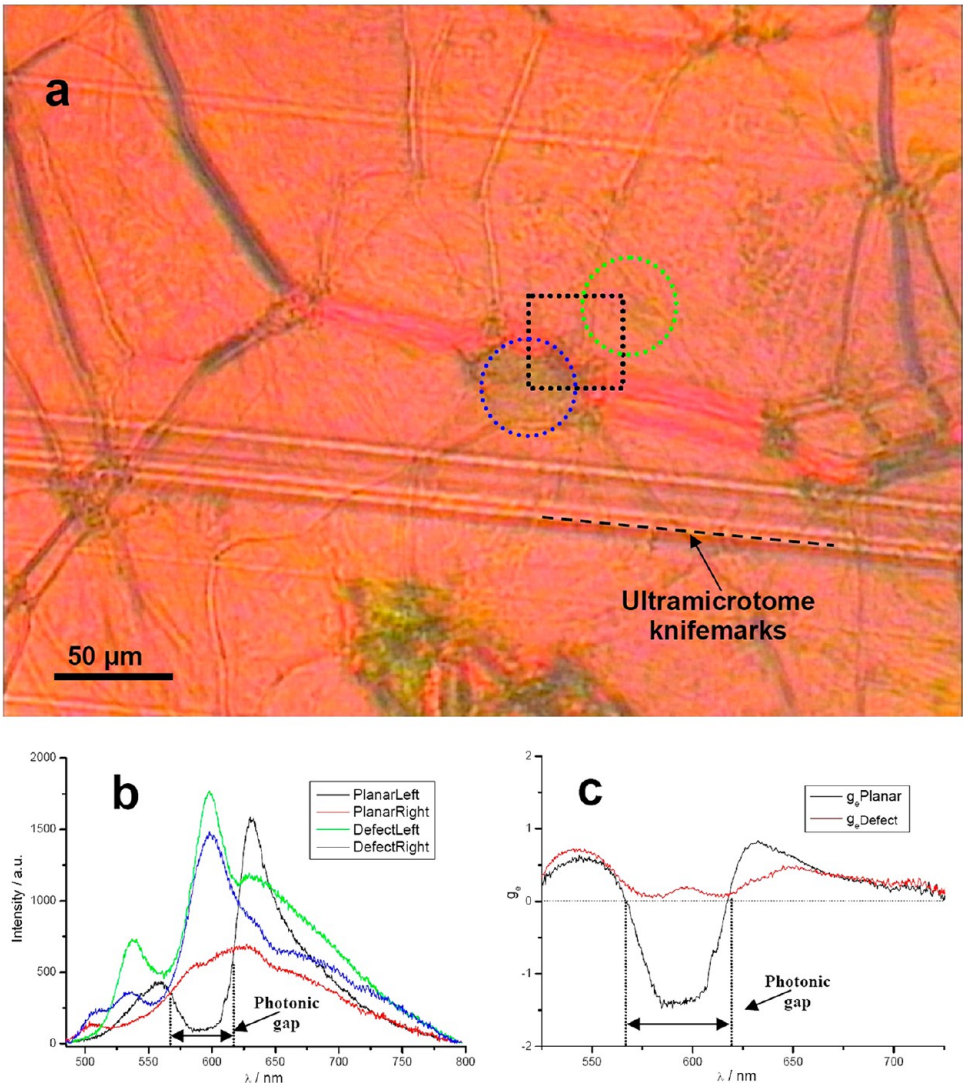

Figure 2. Analysis of the influence of aggregation of QDs embedded in a CLC matrix on their fluorescence characteristics. (a) A polarized optical microscopy (POM) image of the ultramicrotomed area of the surface of the QD−CLC material. The green circle shows a defect-free area of the material, and the blue circle shows a defect area of the sample. The black square shows the AFM-scanned area (see Figure 3a) containing both planar and defect parts. The diameter of the exciting laser spot is 4 μm. (b) The right- and left-handed circularly polarized components of the fluorescence emission spectra of QDs embedded in the CLC matrix recorded from the areas marked with the green circle (a defect-free, planar area) and the blue circle (a defect area) in (a). Considerable modulation of the left-handed circularly polarized component of the QD fluorescence emission spectrum in the area of the peak of selective light reflection in the LC matrix (λ = 590 nm) is characteristic of the planar area. This modulation is not pronounced in the defect area of the material. (c) Fluorescence dissymmetry factors (g_e, eq 1) for the QDs embedded in the planar and defect zones of the CLC matrix. The planar zone of the CLC−QD material is characterized by a highly negative g_e, which is an indicator of a good quality of the material.

3D reconstructions of the QD distribution in the CLC matrix in both planar and defect zones of this area of the sample (Figure 3b,c). The sectioning plane was perpendicular to the CLC helix axis, so that we observed much less of the characteristic background topography relief that would otherwise considerably complicate the reconstruction of the 3D distribution of individual QDs. Figure 3d shows one of the AFM images used for serial 3D reconstruction of the QD distribution in the planar area (Figure 3b). Here, one can clearly see two individual QDs. A cross-section of this AFM topography image shown in Figure 3e proves that here we observe separate individual QDs, because their height does not exceed 10 nm, which corresponds to the diameter of a QD with a TOPO shell partly embedded in the CLC matrix. Analysis of the SPNT data shown in Figure 3c demonstrated that the QDs in the defect zone were aggregated in miniclusters with an average diameter of about 1.5 μm. Supplementary Figure S1 shows typical AFM images and corresponding cross sections of QD miniclusters in the defect zone. Although the sizes of these miniclusters were much less than the total thickness of the CLC matrix, they proved to be sufficiently large to destroy the planar structure in this area of the sample (Figure 2). We used the following routine for the

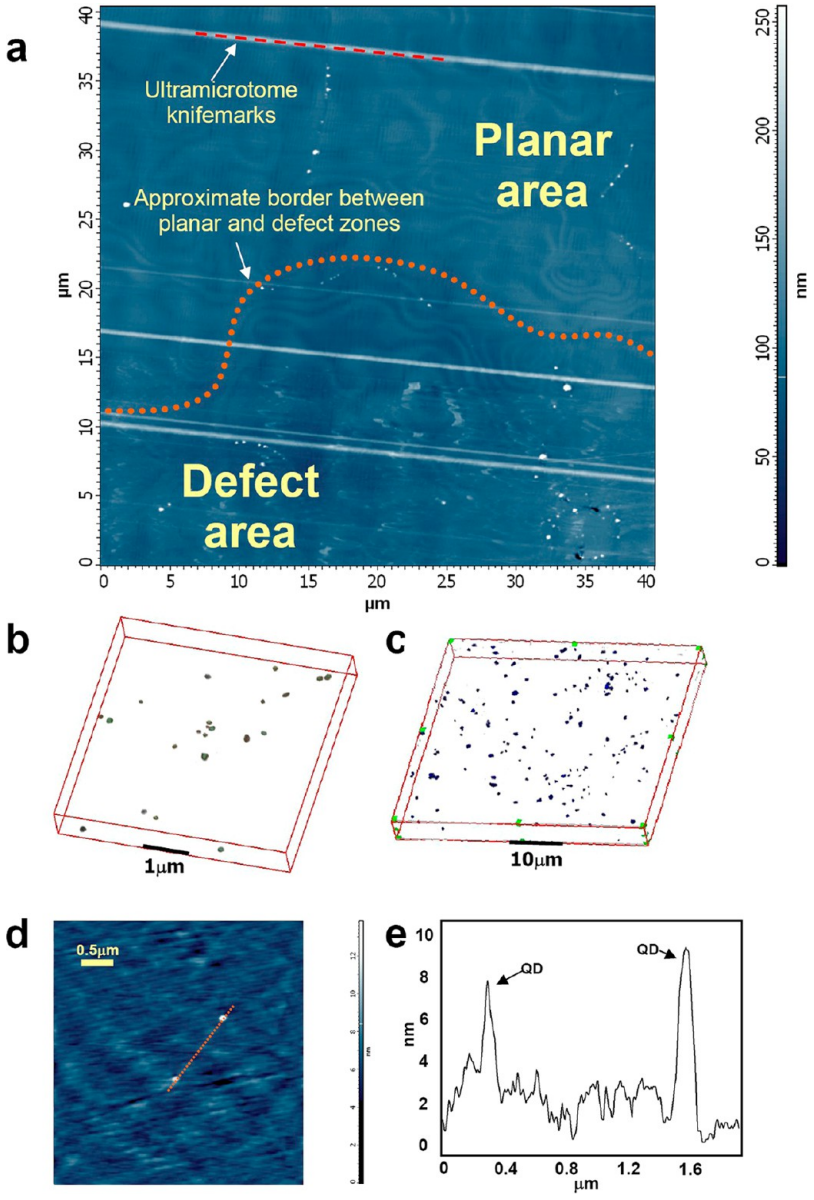

Figure 3. Structural analysis of the 2D and 3D distributions of QDs embedded in the planar and defect areas of a CLC matrix. (a) A 2D AFM image of the QD−CLC sample area (40 × 40 μm) including both planar and defect areas. (b) An SPNT 3D reconstruction of the QD distribution in the planar area of the QD−CLC material. Homogeneous distribution of individual QDs is observed. The Z axis corresponds to the cholesteric helix axis of the LC matrix. The size of the reconstructed sample is 5.0 × 5.0 × 0.7 μm. (c) The 3D distribution of QD clusters in the defect area of the QD−CLC material reconstructed by means of SPNT. The *Z* axis corresponds to the cholesteric helix axis of the LC matrix. The size of the reconstructed sample is 50 × 50 × 5.0 μm. (d) A 2D AFM image of the planar area of the QD−CLC material where QDs are not clustered. This is one of the images used for the 3D reconstruction shown in (b). (e) A cross-section profile of the AFM image (d) along the dotted line.

evaluation of the amount and concentration of homogeneously distributed QDs and the corresponding value of their solubility in the CLC-matrix based on the SPN data shown in Figure 3.

The mass fraction of homogeneously dissolved particles could be described as

$$w_{homo} = (\rho/\rho_0)Nv_{QD} \quad (2)$$

where ρ = 5.8 g/cm^3 is the density of the CdSe core, which is an approximation of the overall density of the CdSe/ZnS core/shell QD; $\rho_0 \approx 1$ g/cm^3 is the density of the CLC matrix; $v_{QD} = 1.715 \times 10^{-25}$ m^3 is the mean volume of a QD without the TOPO shell, whose weight is much less than that of the CdSe core (the density of TOPO is 0.88 g/cm^3); and N is the volume concentration of QDs in the sample. N was calculated as

$$N = (N_{obs}/V)(h/d_{QD}) \quad (3)$$

where N_{obs} is the counted number of QDs in the analyzed 3D-reconstructed volume (according to Figure 3b, N_{obs} = 22); h = 50 nm is the thickness of the ultramicrotome section; V = 17.5 um^3 is the sample volume (Figure 3b); and $d_{QD} \approx 10$ nm is the mean diameter of a QD with the TOPO shell. Therefore, we

could calculate the volume concentration of homogeneously dissolved QDs in the analyzed sample as $N = (6.28 \pm 1.33) \cdot 10^{18}$ m^{-3}. Thus, according to eq 1, the homogeneous solubility of QDs in the CLC matrix (w_{homo}) was $(6.25 \pm 1.32) \cdot 10^{-4}$ wt %. Given an initial mass fraction of the embedded QDs of 0.25 wt %, one can see that only one out of 40 embedded QDs was dissolved in the CLC matrix homogeneously.

Analysis of the POM images and integrated fluorescence spectra recorded from a large area of the QD−CLC material, at the diameter of the excitation laser spot of 2 mm, proved that the major part of the QD−CLC sample had a planar structure without defects.[12,13] This can be explained by the fact that, although most QDs (>97%) were aggregated in clusters, the defect areas containing the clusters were very compact and occupied only a small part of the total volume of the QD−CLC sample. Hence, their presence did not distort the macroscopic optical properties of the material.

Regarding the engineering of the hybrid optical devices where the QD fluorescence is modulated by the CLC matrix, it is evident that the main disadvantage of the QD−CLC system is a very low concentration of homogeneously dissolved QDs, which leads to a low light emission by these structures. At the same time, the defects caused by QD incorporation have almost no effect on the integrated optical properties of the material. Therefore, our data show that the development of novel surfactants that could be substituted for TOPO on the surface of QDs and increase its solubility is the most important challenge in the development of future optical devices based on fluorescent QDs embedded in CLC matrices.

The last but not least result obtained using the novel SPNT−OM technique concerns the influence of a single QD on the planar structure of the CLC matrix in the vicinity of the nanocrystal. Although the results described above show that the overall planar structure of the CLC matrix is not disturbed in the zones of homogeneous QD distribution, it is still possible that the structure is affected locally, in the close vicinity of each QD, but is recovered with increasing distance from it. This question is crucial for determination of the maximum possible concentration of individual QDs in the matrix: the smaller the defect area around each QD, the higher QD concentration can be used without disturbing the overall planar matrix structure. To answer this question, we performed an SPNT 3D reconstruction of a QD−CLC sample in the planar zone, with the section plane parallel to the helix axis of the material (Figure 4). This allowed us to observe the characteristic periodic structure on the surface corresponding to the pitch of the cholesteric helix structure. Figure 4a shows the reconstructed 3D SPNT image of the QD−CLC structure in the area of homogeneous QD distribution. No aggregation of QDs or distortion of the CLC planar structure similar to those described earlier[23−25] are visible in this image. Nor are there any distortions in the 2D AFM

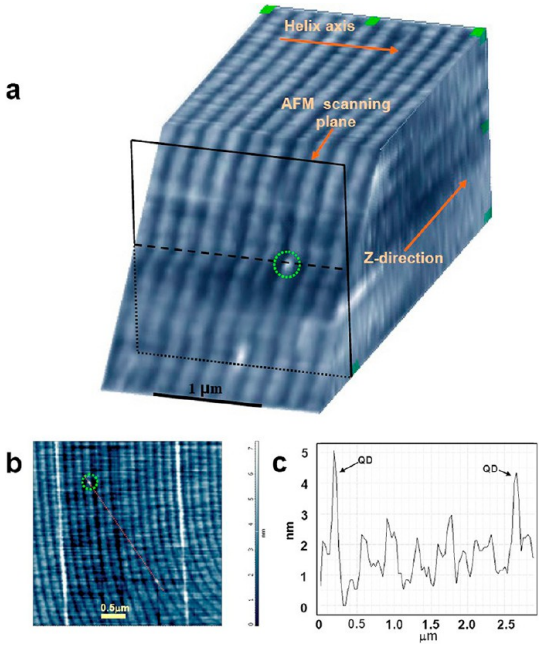

Figure 4. Influence of individual QDs on the planar structure of the CLC matrix. (a) An SPNT 3D reconstruction of the periodic structure of the CLC matrix doped with QDs in the planar area of the sample. The *Z* direction is perpendicular to the cholesteric helix axis of the CLC-matrix. The green circle indicates one of the individual QDs embedded in the matrix. (b) One of 2D AFM images used for the 3D reconstruction shown in (a); the green circle indicates the same individual QD as in (a). (c) A cross-section profile of the AFM image (b) along the dotted line.

images of the CLC planar structure in the vicinities of individual QDs (Figure 4b,c). Therefore, one may conclude that, by using suitable surfactants, the volume concentration of homogeneously distributed QDs may be strongly increased without considerable distortion of the planar structure of the CLC matrix. For our samples, estimations show that the average distance between individual QDs is about 150 nm, which means that the volume concentration of QDs in the CLC matrix can be increased by at least an order of magnitude.

The strategic nanoscience and nanotechnology development strongly requests applications of advanced combined techniques, which would permit direct quantitative correlation of the nanoscale material structure with its microscopic optical characteristics. Correlative light and electron microscopy (CLEM) combining optical microscopy and electron tomography (ET),[26,27] also referred to as 3D TEM, is a good candidate for such a technique. An alternative approach to volume reconstruction is the so-called slice-and-view method, in which the 3D morphology is analyzed by repetitively cutting away some material from the sample by the focused ion beam (FIB) technique and subsequently imaging the fresh surface by means of SEM.[28,29] Although these techniques have proved to be versatile tools for nanoscale 3D reconstruction of biological and polymer materials,[30−34] they may cause

a damage of the sample by electron radiation; in addition, the thickness of the analyzed section in the case of ET is limited to 100−300 nm (the maximal depth of 3D analysis).

In contrast to electron microscopy, scanning probe microscopy (SPM) can be regarded as a nondestructive technique for soft-matter surface analysis.[35,36] It was recently combined with optical microspectroscopy for 2D structural and optical analyses of the same sample area,[37,38] but it cannot be used to study the 3D structure of the sample on the nanoscale. Recently, SPM was combined with ultramicrotomy in an integrated device for 3D-nanotomography.[39−42] In this case, consecutive SPM measurements can be performed immediately after each microtome section at the fresh surface of an untreated block face[43,44] in a way similar to the FIB−SEM slice-and-view approach. Therefore, the depth resolution of the 3D reconstruction by scanning probe nanotomography (SPNT) is limited only by the thickness of the sections removed from the block face surface and may be as fine as 10 nm. Moreover, the block face surface can be analyzed using a variety of SPM modes, such as phase imaging, current distribution measurements (conductive atomic force microscopy, C-AFM),[39,40] magnetic[45] or electrostatic force microscopy (EFM),[39] force curve measurements, and chemical force microscopy.[46,47] Therefore, SPNT makes it possible to simultaneously study the 3D spatial organization of a material, distribution of morphological features, and some local properties (mechanical, electrical, magnetic, and chemical ones) of the material. SPNT combines 3D reconstruction using a new methodology and unique instrumentation with characterization of the corresponding functional properties of soft matter[42] and can be applied to serial section tomography of a wide range of soft biological and polymer materials at room[40] and cryogenic temperatures.[41] Note that, in principle, this technique places no limitation on the thickness of the sample analyzed. The SPNT technique has been successfully applied to studying the 3D structures of biological objects and different advanced materials, such as polymer blends and polymer−nanotube[40] and polymer−graphene[39] nanocomposites. However, this methodology has not been combined with correlative optical microscopy required for comprehensive analysis of the 3D nanostructure and optical properties of nanohybrid materials.

CONCLUSION

We have developed a correlative microscopy SPNT−OM setup for obtaining SPM and OM data and nanoscale 3D-reconstruction for the same area of the sample. This technique provides a depth resolution of the 3D reconstruction as fine as 10 nm at the total thickness of the sample up to 250 μm. At the same time, the optical and morphological properties of a nanomaterial may be investigated in parallel using practically all modes of optical microscopy and spectroscopy, as well as a variety of SPM modes, at each step of the 3D reconstruction.

The novel SPNT−OM technique has been used to investigate the optical and morphological properties of nanohybrid materials based on a low-molecular-weight cholesteric LC matrix doped with fluorescent CdSe/ZnS QDs. It has been shown that the maximal mass fraction of homogeneously dissolved QDs in the CLC matrix is $6.25 \pm 1.32 \times 10^{-4}$ wt %; *i.e.*, only one out of 40 embedded QDs was dissolved in the CLC matrix homogeneously. The other QDs (>97%) have been found to be organized in miniclusters with an average diameter of about 1.5 μm because of the low affinity of the QD surface for the CLC matrix. Analysis of the microscopic and spectroscopic data on the areas with homogeneous distribution and clustering of QD has shown that the defect areas containing the clusters are very compact and occupy only a small part of the total volume of the QD−CLC sample. The major part of the QD−CLC sample has a planar structure and is characterized by a highly negative QD fluorescence dissymmetry factor ($g_e \approx 1.5$), which is an indicator of a good quality of the material. The effect of homogeneously dissolved individual QDs on the texture of the CLC matrix has been explored by means of 3D-reconstruction of the CLC planar structure in the area of homogeneous QD distribution. We have found that the CLC planar texture is not distorted in the vicinity of individual QDs. The average distance between individual QDs has been found to be about 150 nm, which allows the volume concentration of QDs in the CLC matrix to be increased by at least an order of magnitude, thereby enhancing the QD-related properties of the hybrid material without disruption of its structure.

The novel technique is expected to provide important data on the effects of nanoparticles on the structural organization of organic and LC matrices and biomedical materials. Therefore, it may become an important tool for characterization and quality control of nanotechnological fabrication processes and products in the cases where polymer or liquid crystal matrices, biomedical materials (pharmaceutical preparations and drug delivery systems), or biological objects (tissues, cells, and microorganisms) contain semiconductors, metallic or carbon nanoparticles, or nanoclusters.

MATERIALS AND METHODS

SPNT−OM Setup and Measurements. *SPNT Setup.* For SPNT measurements and 3D reconstruction, an NTEGRA-Tomo system (NT-MDT Co., Russia) was used, which comprised an SPM combined with a Leica EM UC6NT ultramicrotome (Leica Microsystems GmbH, Austria) on a MOD-1 active vibration-protective table

(Halcyonics GmbH, Germany).[48] The SPM measuring head in the tip-scanning configuration was mounted on the ultramicrotome knife holder over an Ultra AFM 35 diamond knife (Diatome AG, Switzerland). This construction allowed examining the sample surface with the SPM tip in a semicontact mode immediately after sectioning, when the ultramicrotome arm was in the highest position. The cantilever tips used for AFM measurements were NSC15 (Micromash, Estonia) with a characteristic resonant frequency of about 325 kHz; the radius was smaller than 10 nm. The 512 × 512 pixel AFM images were acquired with a scanning rate of 1 Hz (~8.5 min per image). The cantilever free oscillation amplitude was set to 40 nm, with the set point at 50% of the free amplitude, and the integral feedback gain was 0.4.

SPM−OM setup. The SPM head (SMENA, NT-MDT, Russia) was mounted on the same optical table in the manner that allows the placement of the SPM probe tip within several micrometers from the optical axis. The spot of an LGN-519M Ar^+ laser (OAO Plazma, Ryazan, Russia) used for sample irradiation was adjusted to the same spatial area through the deflectometer mirror of the SPM head as shown in Supplementary Figure 1. All optical images were obtained with an Optem Zoom 125C upright microscope adjusted to the common optical axis passing through the same point as the SPM probe tip. The cross-polarized illumination system consisted of an ACE Light Source, a homemade condenser lens system, a linearly polarizing polymer film (serving as a polarizer) placed directly on the condenser at an arbitrary or fixed angle, and a similar film (serving as an analyzer) placed into a rotatable CCD−microscope coupler. The fluorescence spectra were recorded using an M266 automated monochromator/spectrograph (SOLAR Laser Systems, Minsk, Belarus) with a CCD U2C-16H7317 (Ormins, Minsk, Belarus) and a homemade light-collecting system with two Semrock 488-nm RazorEdge ultrasteep long-pass edge filters (Rochester, NY, USA). The aforementioned Ar^+ laser operating at 488 nm was used for fluorescence excitation at a light intensity of 0.063 mW as measured with a LaserMate-Q (Coherent) intensity meter, with the beam focused onto a spot with a diameter of about 30 μm. The fluorescence spectra were recorded in an inverted mode with the use of a 20×/0.40 LCPlanFl lens (Olympus, Japan) and the homemade confocal unit with two 100 mm objective lenses and 100 μm pinhole.

A step-by-step measurement scheme is shown in Figure 1.

Step 1. Initial ultramicrotome sectioning of the LC films on a glass substrate was performed with the use of the ultramicrotome in the SPNT setup. The area of the sectioned block face was no more than 1 mm^2 in order to simplify the location of the same area for complementary microscopic studies.

Step 2. The POM images, fluorescence spectra, and 2D AFM images of the microtomed block face surface of the sample were obtained with the use of the combined SPM−OM setup described above. The sample sectioned at step 1 was placed directly on the top of the table for inverted optical microscopy with an open optical axis. 2D AFM images were obtained using the aforementioned SPM head; these images were used to locate the same area for SPNT 3D reconstruction at the next step.

Step 3. The area that had been analyzed by means of AFM−POM at the previous steps was located using optical microscopy and AFM, and the 3D structure of this area was reconstructed by the SPNT technique. The 3D reconstruction was obtained by means of sample surface imaging alternated with serial ultramicrotoming. The minimum section thickness used in this study was 50 nm. The ImagePro Plus 6.0 postprocessing software (Media Cybernetics, Inc.) with a 3DConstructor option for the automated image alignment and visualization of 3D images was used for the reconstruction.

For 3D reconstruction of the periodic structure of the CLC matrix doped with QDs, a QD−CLC mixture was deposited on a PTFT substrate, embedded in epoxy resin, and ultramicrotomed in the plane parallel to the helix axis. Then, a series of ultramicrotome sections with the same section thickness, each followed by AFM measurements, were performed.

Chemicals. Cyclosiloxane (SilBlue) was purchased from Wacker Chemie (Munich, Germany). The chiral photochromic dopant 2,5-bis(4-methoxycinnamoyl)-1,4;3,6-dianhydro-D-sorbitol (Sorb) was synthesized as described in our previous study.[49]

Synthesis of Quantum Dots. CdSe/ZnS core/shell QDs were synthesized as described earlier.[50,51] Here, we used homogeneous QDs (size deviation, 10%) with CdSe cores approximately 5 nm in diameter (for QDs with emission at 604 nm) with approximately two monolayers of the ZnS shell[52] and a quantum yield exceeding 60%. The synthesized QDs contained TOPO/TOP surfactants on their surface.[53] The QD photoluminescence was found to be stable during photopolymerization and fluorescence excitation, with the variation of photoluminescence emission during photopolymerization not exceeding 10%.

Material and Cell Preparations. QD−CLC materials were prepared by dissolving SilBlue (96.3 wt %), Sorb (3.2 wt %), QDs with $\lambda_{max} \sim 530$ nm (0.05 wt %), and QDs with $\lambda_{max} \sim 604$ nm (0.5 wt %) in chloroform, slowly evaporating the solvent, and drying the material in a vacuum at 120 °C. Aggregation and phase separation did not occur during the mixture preparation, and the resultant mixtures were homogeneous. The absence of relatively large aggregates of nanoparticles was confirmed by fluorescent and polarized optical microscopy. Dissolving of QDs did not lead to any noticeable changes in the optical quality of planar-oriented films, which remained transparent.

For optical and morphological studies, 20-μm films sandwiched between two flat glass plates were prepared. The thickness of the test samples was controlled with Teflon spacers. In order to obtain a good planar texture, we used the LC photoalignment technique.[54] Glass plates were spin-coated with 2 mg/mL of the sodium salt of poly[1-[4-(3-carboxy-4-hydroxy-phenylazo)benzenesulfonamido]-1,2-ethanediyl (Sigma-Aldrich, St. Louis, MO, USA). After drying at room temperature, the glass plates coated with this polymer were irradiated with polarized polychromatic light by means of a mercury lamp (~15 mW/cm^2, 30 min). A Glan−Taylor prism was used as a polarizer.

The planar texture of QD−CLC was obtained by annealing the samples, which were heated to temperatures well above the glass transition temperature (140 °C). After 30 min of annealing at the same temperature, two glass substrates were separated by shearing. As a result, two glass plates covered with a polymeric film were obtained. They were annealed for about another 30 min and then slowly cooled to room temperature at a rate of 1 °C/min using a Mettler hot stage. After irradiation of the QD−CLC sample prior to the absorbance and fluorescence measurements, the samples were annealed for about 20 min and slowly cooled to room temperature at a rate of 1 °C/min.

Study of Phase Behavior and Optical and Electro-optical Analyses. The phase transition temperatures of the mixtures were determined using a LOMO P-112 polarizing optical microscope (St. Petersburg, Russia) equipped with a Mettler TA-400 hot stage (Mettler-Toledo, Greifensee, Switzerland). The transmittance spectra of planar-oriented films were recorded using a Unicam UV-500 UV−vis spectrophotometer (Thermo Fisher Scientific, Waltham, MA, USA).

Conflict of Interest: The authors declare no competing financial interest.

Acknowledgment. This study was partly supported by the European Commission through the FP7 Cooperation Program (Grant No. NMP-2009-4.0-3-246479), Ministry of Higher Education and Science of the Russian Federation (Grant Nos. 1. G34.31.0050 and 8842) and the Russian Foundation for Basic Research (Grant Nos. 13-04-00168, 11-03-01046, 12-03-00553-a, and 11-02-00369-a). I.N. acknowledges the programs HYNNOV and Nano'Mat supported by the Champagne-Ardenne region, the DRRT Champagne-Ardenne, and the FEDER. We thank Vladimir Ushakov for the help in the preparation of the manuscript.

Supporting Information Available: Figure S1 shows 2D AFM images of QD-clusters in QD-CLC defect sample area and cross-section profiles recorded for these AFM images.

This material is available free of charge *via* the Internet at http://pubs.acs.org.

REFERENCES AND NOTES

1. Dukes, M. J.; Peckys, D. B.; de Jonge, N. Correlative Fluorescence Microscopy and Scanning Transmission Electron Microscopy of Quantum-Dot-Labeled Proteins in Whole Cells in Liquid. *ACS Nano* **2010**, *4*, 4110–4116.
2. Sharma, S.; Rasool, H. I.; Palanisamy, V.; Mathisen, C.; Schmidt, M.; Wong, D. T.; Gimzewski, J. K. Structural-Mechanical Characterization of Nanoparticle Exosomes in Human Saliva, Using Correlative AFM, FESEM, and Force Spectroscopy. *ACS Nano* **2010**, *4*, 1921–1926.
3. Parent, L. R.; Robinson, D. B.; Woehl, T. J.; Ristenpart, W. D.; Evans, J. E.; Browning, N. D.; Arslan, I. Direct *in Situ* Observation of Nanoparticle Synthesis in a Liquid Crystal Surfactant Template. *ACS Nano* **2012**, *6*, 3589–3596.
4. Cong, C.; Yu, T.; Saito, R.; Dresselhaus, G. F.; Dresselhaus, M. S. Second-Order Overtone and Combination Raman Modes of Graphene Layers in the Range of 1690–2150 cm^{-1}. *ACS Nano* **2011**, *5*, 1600–1605.
5. Garreau, A.; Massuyeau, F.; Cordier, S.; Molard, Y.; Gautron, E.; Bertoncini, P.; Faulques, E.; Wery, J.; Humbert, B.; Bulou, A.; *et al.* Color Control in Coaxial Two-Luminophore Nanowires. *ACS Nano* **2013**, *7*, 2977–2987.
6. Fan, Z.; Shelton, M.; Singh, A. K.; Senapati, D.; Khan, S. A.; Ray, P. C. Multifunctional Plasmonic Shell–Magnetic Core Nanoparticles for Targeted Diagnostics, Isolation, and Photothermal Destruction of Tumor Cells. *ACS Nano* **2012**, *6*, 1065–1073.
7. Farokhzad, O. C.; Langer, R. Impact of Nanotechnology on Drug Delivery. *ACS Nano* **2009**, *3*, 16–20.
8. Caplan, J.; Niethammer, M.; Taylor, li, R. M.; Czymmek, K. J. The Power of Correlative Microscopy: Multi-Modal, Multi-Scale, Multi-Dimensional. *Curr. Opin. Struct. Biol.* **2011**, *21*, 686–693.
9. Davidson, M. W.; Abramowitz, M. Optical Microscopy. In *Encyclopedia of Imaging Science and Technology*; John Wiley & Sons, Inc.: New York, 2002.
10. Van Tendeloo, G.; Bals, S.; Van Aert, S.; Verbeeck, J.; Van Dyck, D. Advanced Electron Microscopy for Advanced Materials. *Adv. Mater.* **2012**, *24*, 5655–5675.
11. Glatzel, T.; Hölscher, H.; Schimmel, T.; Baykara, M. Z.; Schwarz, U. D.; Garcia, R. Advanced Atomic Force Microscopy Techniques. *Beilstein J. Nanotechnol.* **2012**, *3*, 893–894.
12. Bobrovsky, A.; Mochalov, K.; Oleinikov, V.; Shibaev, V. Glass-Forming Photoactive Cholesteric Oligomers Doped with Quantum Dots: Novel Materials with Phototunable Circularly Polarised Emission. *Liq. Cryst.* **2011**, *38*, 737–742.
13. Bobrovsky, A.; Mochalov, K.; Oleinikov, V.; Sukhanova, A.; Prudnikau, A.; Artemyev, M.; Shibaev, V.; Nabiev, I. Optically and Electrically Controlled Circularly Polarized Emission from Cholesteric Liquid Crystal Materials Doped with Semiconductor Quantum Dots. *Adv. Mater.* **2012**, *24*, 6216–6222.
14. Lukishova, S. G.; Bissell, L. J.; Winkler, J.; Stroud, C. R. Resonance in Quantum Dot Fluorescence in a Photonic Bandgap Liquid Crystal Host. *Opt. Lett.* **2012**, *37*, 1259–1261.
15. Tong, X.; Zhao, Y. Liquid-Crystal Gel-Dispersed Quantum Dots: Reversible Modulation of Photoluminescence Intensity Using an Electric Field. *J. Am. Chem. Soc.* **2007**, *129*, 6372–6373.
16. Lukishova, S. G.; Bissell, L. J.; Stroud, C. R., Jr.; Boyd, R. W. Room-Temperature Single Photon Sources With Definite Circular and Linear Polarizations. *Opt. Spectrosc.* **2010**, *108*, 417–424.
17. Philippe, G.; Barry, S.; Jelena, V. Focus on Single Photons on Demand. *New J. Phys.* **2004**, 6.
18. Kopp, V. I.; Fan, B.; Vithana, H. K. M.; Genack, A. Z. Low-Threshold Lasing at the Edge of a Photonic Stop Band in Cholesteric Liquid Crystals. *Opt. Lett.* **1998**, *23*, 1707–1709.
19. Shibaev, V.; Bobrovsky, A.; Boiko, N. Photoactive Liquid Crystalline Polymer Systems with Light-Controllable Structure and Optical Properties. *Prog. Polym. Sci.* **2003**, *28*, 729–836.
20. Bobrovsky, A. Y.; Boiko, N. I.; Shibaev, V. P.; Wendorff, J. H. Cholesteric Mixtures with Photochemically Tunable, Circularly Polarized Fluorescence. *Adv. Mater.* **2003**, *15*, 282–287.
21. Blinov, L. M.; Chigrinov, V. G. *Electrooptic Effects in Liquid Crystal Materials*; Springer Verlag: New York, 1993.
22. Bobrovsky, A.; Shibaev, V.; Stumpe, J. Cholesteric Polymer Guest–Host Mixture with Circularly Polarized Fluorescence: Two Ways for Phototuning of Polarization and Its Intensity. *J. Phys. Chem. A* **2006**, *110*, 2331–2336.
23. Agez, G.; Bitar, R.; Mitov, M. Color Selectivity Lent to a Cholesteric Liquid Crystal by Monitoring Interface-Induced Deformations. *Soft Matter* **2011**, *7*, 2841–2847.
24. Boudet, A.; Mitov, M.; Bourgerette, C.; Ondarçuhu, T.; Coratger, R. Glassy Cholesteric Structure: Thickness Variation Induced by Electron Radiation in Transmission Electron Microscopy Investigated by Atomic Force Microscopy. *Ultramicroscopy* **2001**, *88*, 219–229.
25. Meister, R.; Hallé, M. A.; Dumoulin, H.; Pieranski, P. Structure of the Cholesteric Focal Conic Domains at the Free Surface. *Phys. Rev. E* **1996**, *54*, 3771–3782.
26. Mironov, A. A.; Beznoussenko, G. V. Correlative Microscopy: a Potent Tool for the Study of Rare or Unique Cellular and Tissue Events. *J. Microsc. (Oxford, U. K.)* **2009**, *235*, 308–321.
27. Spiegelhalter, C.; Tosch, V.; Hentsch, D.; Koch, M.; Kessler, P.; Schwab, Y.; Laporte, J. From Dynamic Live Cell Imaging to 3D Ultrastructure: Novel Integrated Methods for High Pressure Freezing and Correlative Light-Electron Microscopy. *PLoS One* **2010**, *5*, e9014.
28. Al-Abboodi, A.; Fu, J.; Doran, P. M.; Chan, P. P. Y. Three-Dimensional Nanocharacterization of Porous Hydrogel with Ion and Electron Beams. *Biotechnol. Bioeng.* **2013**, *110*, 318–326.
29. Holzer, L.; Indutnyi, F.; Gasser, P. H.; Münch, B.; Wegmann, M. Three-Dimensional Analysis of Porous BaTiO3 Ceramics Using FIB Nanotomography. *J. Microsc. (Oxford, U. K.)* **2004**, *216*, 84–95.
30. Midgley, P. A.; Dunin-Borkowski, R. E. Electron Tomography and Holography in Materials Science. *Nat. Mater.* **2009**, *8*, 271–280.
31. Medalia, O.; Weber, I.; Frangakis, A. S.; Nicastro, D.; Gerisch, G.; Baumeister, W. Macromolecular Architecture in Eukaryotic Cells Visualized by Cryoelectron Tomography. *Science* **2002**, *298*, 1209–1213.
32. Milne, J. L. S.; Subramaniam, S. Cryo-electron Tomography of Bacteria: Progress, Challenges and Future Prospects. *Nat. Rev. Microbiol.* **2009**, *7*, 666–675.
33. Möbus, G.; Inkson, B. J. Nanoscale Tomography in Materials Science. *Mater. Today (Oxford, U. K.)* **2007**, *10*, 18–25.
34. van Bavel, S. S.; Loos, J. Volume Organization of Polymer and Hybrid Solar Cells as Revealed by Electron Tomography. *Adv. Funct. Mater.* **2010**, *20*, 3217–3234.
35. Binnig, G.; Ch, G.; Stoll, E.; Albrecht, T. R.; Quate, C. F. Atomic Resolution with Atomic Force Microscope. *EPL* **1987**, *3*, 1281.
36. Magonov, S. N.; Reneker, D. H. Characterization of Polymer Surfaces with Atomic Force Microscopy. *Annu. Rev. Mater. Sci.* **1997**, *27*, 175–222.
37. Colombelli, J.; Besser, A.; Kress, H.; Reynaud, E. G.; Girard, P.; Caussinus, E.; Haselmann, U.; Small, J. V.; Schwarz, U. S.; Stelzer, E. H. K. Mechanosensing in Actin Stress Fibers Revealed by a Close Correlation Between Force and Protein Localization. *J. Cell Sci.* **2009**, *122*, 1665–1679.
38. Labernadie, A.; Thibault, C.; Vieu, C.; Maridonneau-Parini, I.; Charrière, G. M. Dynamics of Podosome Stiffness Revealed by Atomic Force Microscopy. *Proc. Natl. Acad. Sci. U. S. A.* **2010**, 10.1073/pnas.1007835107.
39. Alekseev, A.; Chen, D.; Tkalya, E. E.; Ghislandi, M. G.; Syurik, Y.; Ageev, O.; Loos, J.; de With, G. Local Organization of Graphene Network Inside Graphene/Polymer Composites. *Adv. Funct. Mater.* **2012**, *22*, 1311–1318.
40. Alekseev, A.; Efimov, A.; Lu, K.; Loos, J. Three-Dimensional Electrical Property Mapping with Nanometer Resolution. *Adv. Mater.* **2009**, *21*, 4915–4919.

41. Efimov, A. E.; Gnaegi, H.; Schaller, R.; Grogger, W.; Hofer, F.; Matsko, N. B. Analysis of Native Structures of Soft Materials by Cryo Scanning Probe Tomography. *Soft Matter* **2012**, *8*, 9756–9760.
42. Efimov, A. E.; Tonevitsky, A. G.; Dittrich, M.; Matsko, N. B. Atomic Force Microscope (AFM) Combined with the Ultramicrotome: A Novel Device for the Serial Section Tomography and AFM/TEM Complementary Structural Analysis of Biological and Polymer Samples. *J. Microsc. (Oxford, U. K.)* **2007**, *226*, 207–216.
43. Matsko, N.; Mueller, M. AFM of Biological Material Embedded in Epoxy Resin. *J. Struct. Biol.* **2004**, *146*, 334–343.
44. Matsko, N. B. Atomic Force Microscopy Applied to Study Macromolecular Content of Embedded Biological Material. *Ultramicroscopy* **2007**, *107*, 95–105.
45. Hartmann, U. Magnetic Force Microscopy: Some Remarks from the Micromagnetic Point of View. *J. Appl. Phys.* **1988**, *64*, 1561–1564.
46. Noy, A.; Vezenov, D. V.; Lieber, C. M. Chemical Force Microscopy. *Annu. Rev. Mater. Sci.* **1997**, *27*, 381–421.
47. Zlatanova, J.; Lindsay, S. M.; Leuba, S. H. Single Molecule Force Spectroscopy in Biology Using the Atomic Force Microscope. *Prog. Biophys. Mol. Biol.* **2000**, *74*, 37–61.
48. Milette, J.; Cowling, S. J.; Toader, V.; Lavigne, C.; Saez, I. M.; Bruce Lennox, R.; Goodby, J. W.; Reven, L. Reversible Long Range Network Formation in Gold Nanoparticle–Nematic Liquid Crystal Composites. *Soft Matter* **2012**, *8*, 173–179.
49. Bobrovsky, A. Y.; Boiko, N. I.; Shibaev, V. P. New Chiral-Photochromic Dopant with Variable Helical Twisting Power and Its Use in Photosensitive Cholesteric Materials. *Mol. Cryst. Liq. Cryst. Sci. Technol., Sect. A* **2001**, *363*, 35–50.
50. Sukhanova, A.; Devy, J.; Venteo, L.; Kaplan, H.; Artemyev, M.; Oleinikov, V.; Klinov, D.; Pluot, M.; Cohen, J. H. M.; Nabiev, I. Biocompatible Fluorescent Nanocrystals for Immunolabeling of Membrane Proteins and Cells. *Anal. Biochem.* **2004**, *324*, 60–67.
51. Sukhanova, A.; Venteo, L.; Devy, J.; Artemyev, M.; Oleinikov, V.; Pluot, M.; Nabiev, I. Highly Stable Fluorescent Nanocrystals as a Novel Class of Labels for Immunohistochemical Analysis of Paraffin-Embedded Tissue Sections. *Lab. Invest.* **2002**, *82*, 1259–1261.
52. Baranov, A. V.; Rakovich, Y. P.; Donegan, J. F.; Perova, T. S.; Moore, R. A.; Talapin, D. V.; Rogach, A. L.; Masumoto, Y.; Nabiev, I. Effect of ZnS Shell Thickness on the Phonon Spectra in CdSe Quantum Dots. *Phys. Rev. B* **2003**, *68*, 165306.
53. Wargnier, R.; Baranov, A. V.; Maslov, V. G.; Stsiapura, V.; Artemyev, M.; Pluot, M.; Sukhanova, A.; Nabiev, I. Energy Transfer in Aqueous Solutions of Oppositely Charged CdSe/ZnS Core/Shell Quantum Dots and in Quantum Dot–Nanogold Assemblies. *Nano Lett.* **2004**, *4*, 451–457.
54. Bobrovsky, A.; Ryabchun, A.; Shibaev, V. Liquid Crystals Photoalignment by Films of Side-Chain Azobenzene-Containing Polymers with Different Molecular Structure. *J. Photochem. Photobiol., A* **2011**, *218*, 137–142.